

The 28 October 2022 M_w 3.8 Goesan Earthquake Sequence in Central Korea: Stress Drop, Aftershock Triggering, and Fault Interaction

Won-Young Kim^{1,2} , Min-Seong Seo² , Jun Yong Park² , Sangwoo Han² , Young Oh Son² , and YoungHee Kim^{*2} 

ABSTRACT

We identified the causative fault of the 2022 Goesan, Korea, earthquake sequence based on the precise relocation of the sequence that revealed a 0.8 km-long fault plane striking east-southeast–west-northwest. The fault plane encompasses the largest foreshock, the mainshock, and the majority of the aftershocks. The orientation of the fault plane is consistent with the left-lateral strike-slip motion along the east-southeast (106°) striking nodal plane of the focal mechanism. The Jogok fault system recently mapped in the source area runs through the mainshock epicenter with a consistent strike and left-lateral strike-slip motion, which suggests that it is the likely causative fault of the 2022 M_w 3.8 Goesan earthquake sequence. It is a rare case of assigning a causative fault for a small-sized (M_w 3.8) earthquake with some confidence in a typical stable continental region setting, albeit no surface break observed due to deep focal depth (~13 km) and the small size of the event. Aftershocks on the main fault plane, and on the adjacent subparallel fault patches seemed to be triggered by the increase in Coulomb stress caused by the mainshock. Two large aftershocks on the subparallel fault patches show slightly higher stress drops than the large foreshock and mainshock on the main fault plane, likely due to high frictional strength on those fault patches. Events of the 2022 Goesan earthquake sequence progressed rapidly in time and appear to be high stress-drop events compared with other earthquakes that occurred in other regions in Korea, probably due to the long quiescent period in the Goesan earthquake epicentral region.

KEY POINTS

- We identified causative fault of 2022 Goesan, Korea, earthquake sequence in areas of low seismicity.
- The sequence progressed rapidly temporally and to a complex spatial extent through interevent triggering.
- High stress drops of $M_w > 3$ events indicate high frictional fault strength due to the long quiescent period.

Supplemental Material

residents in Korea were aware of the earthquakes within the first minute, because emergency text messages were sent to all residents in Korea via cell phones (over 95% of the population uses). The peak ground acceleration of 6.65 (%g) was registered at Chungju station (CHJ3, AZ = 90°) about 8 km east of the epicenter (Fig. 2), which corresponds to the maximum instrumental intensity V on modified Mercalli intensity (MMI). A total of 168 felt reports were received with the maximum intensity of V (MMI), mostly from areas within the 50 km radius of the epicenter in central Korea, according to KMA.

INTRODUCTION

On 28 October 2022, at 23:28, Korea Meteorological Administration (KMA) issued an earthquake alarm message regarding an M_L 3.5 earthquake that occurred about 11 km northeast of Goesan City located in the south-central Korean Peninsula (Fig. 1). The second alarm message followed within 20 s; this time, the message was for an M_L 4.1 earthquake at the same epicenter. Although minor damages, a dozen cracked walls, and broken windows were reported in Goesan and Chungju cities near the epicenter from these small earthquakes (Fig. 2), most

1. Lamont-Doherty Earth Observatory of Columbia University, Palisades, New York, U.S.A.,  <https://orcid.org/0000-0002-0005-9681> (W-YK); 2. School of Earth and Environmental Sciences, Seoul National University, Seoul, Republic of Korea,  <https://orcid.org/0000-0001-7043-8938> (M-SS);  <https://orcid.org/0000-0003-2244-0210> (JYP);  <https://orcid.org/0000-0001-5832-7127> (SH);  <https://orcid.org/0000-0001-9472-4314> (YOS);  <https://orcid.org/0000-0002-1111-632X> (YHK)

*Corresponding author: younghkim@snu.ac.kr

Cite this article as Kim, W.-Y., M.-S. Seo, J. Y. Park, S. Han, Y. O. Son, and Y. H. Kim (2023). The 28 October 2022 M_w 3.8 Goesan Earthquake Sequence in Central Korea: Stress Drop, Aftershock Triggering, and Fault Interaction, *Bull. Seismol. Soc. Am.* **XX**, 1–16, doi: [10.1785/0120230078](https://doi.org/10.1785/0120230078)

© Seismological Society of America

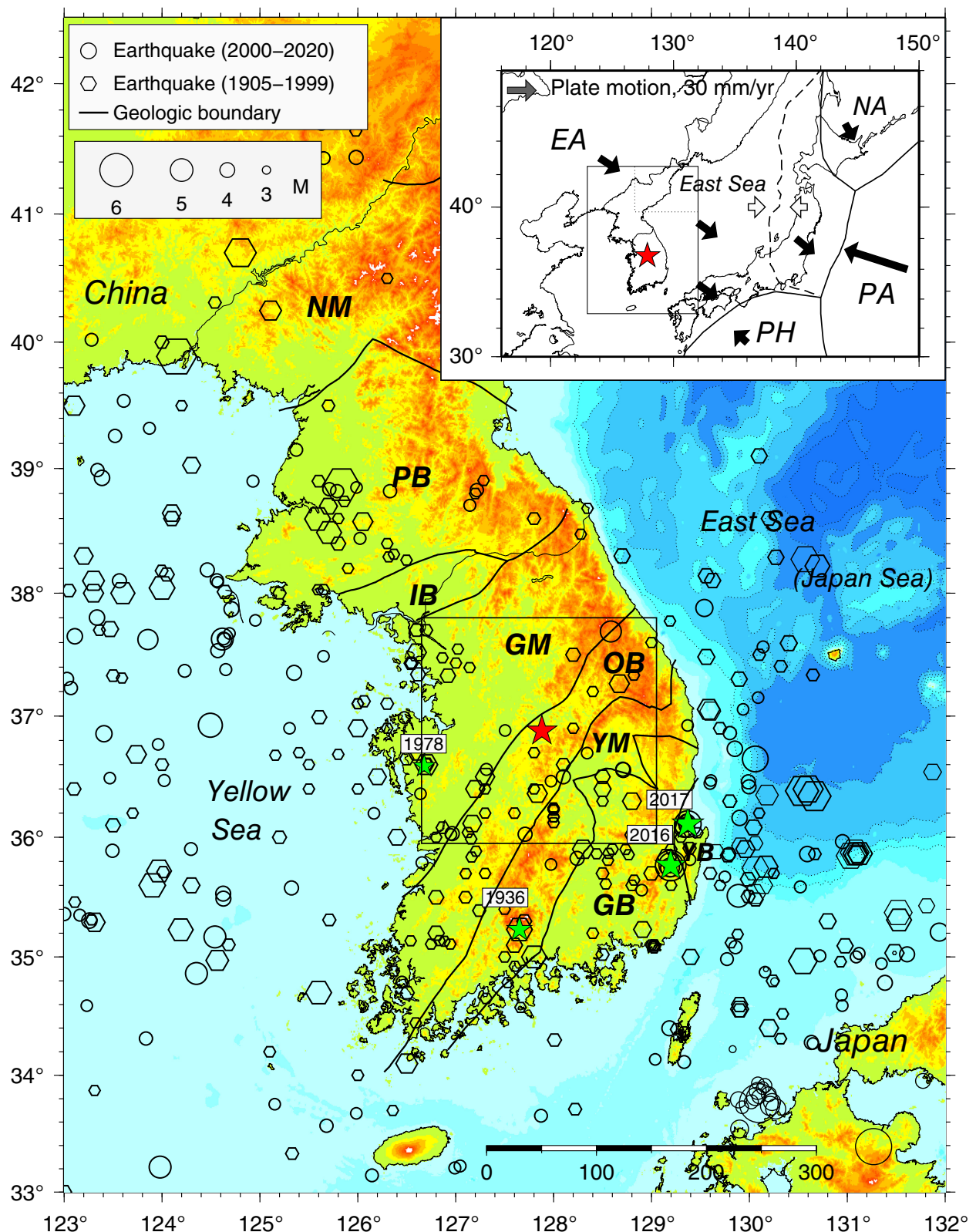


Figure 1. Topographic–bathymetric map of the Korean Peninsula showing seismicity and geologic units. The 28 October 2022 Goesan earthquake is plotted with a red star. Epicenters of shallow earthquakes with $M > 3.5$ that occurred during 1905–1999 are plotted with hexagons and during 2000–2020 are plotted with circles. Significant earthquakes ($M \geq 5$) with reported substantial damage since 1905 are plotted with green stars. Major geologic units in Korean Peninsula are indicated from north to south: GB, Gyeongsang basin

(Mesozoic); GM, Gyeonggi massif; IB, Imjingang belt; NM, Nangrim massif; OB, Ogcheon fold belt; PB, Pyongnam basin; YB, Yeonil basin (Tertiary); YM, Yeongnam massif. The upper-right inset shows tectonic plates and their boundaries: EA, Eurasian; NA, North America; PA, Pacific; and PH, Philippine Sea. The dashed line indicates a possible incipient plate boundary following the proposed Okhotsk Sea plate boundary, according to Bird (2003). The color version of this figure is available only in the electronic edition.

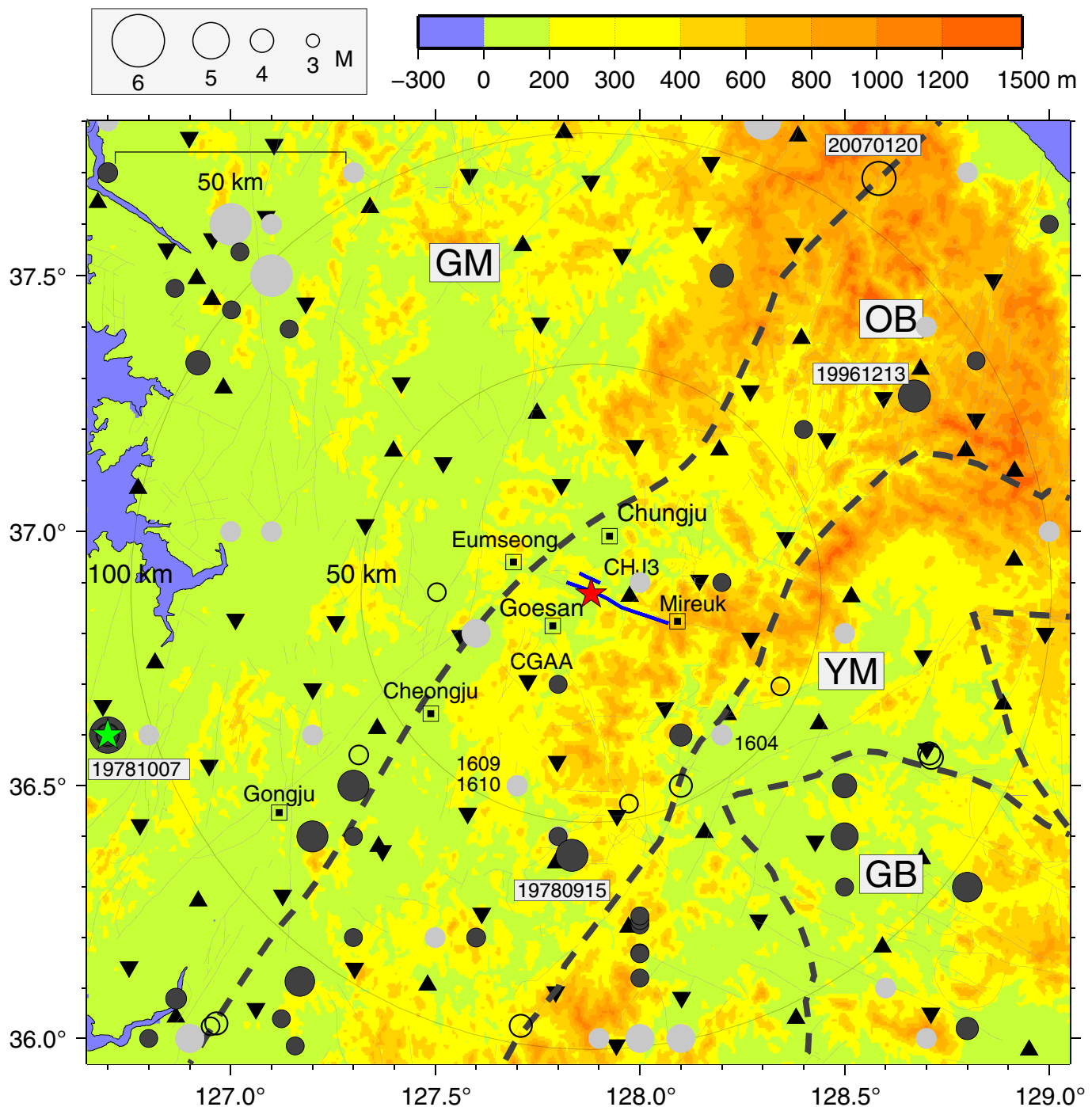


Figure 2. Epicenters, seismographic stations, and mapped faults within a 100 km radius of the Goesan earthquake (red star) in the region outlined by the solid box in Figure 1. Thick black dashed lines indicate major geologic units in Korean Peninsula. Epicentral area is in the Ogneon fold belt (OB). Population centers (cities) near the epicenter are drawn with squares, and their names are annotated. Mapped Jogok fault system (blue solid line) runs through the epicenter between the town of Eumseong and Mireuk (Park, 2005), and thin gray lines are faults in the geologic map (KIGAM, 2019). Broadband and short-period stations are plotted with triangles, and accelerographs are plotted with inverted triangles.

Earthquakes with $M \geq 3.5$ that occurred during 1905–1999 are plotted with black circles, whereas events that occurred during 2000–2020 are plotted with open circles. Historical earthquakes with intensity greater than VI (modified Mercalli intensity [MMI]) during 2–1904 A.D. are plotted with gray circles with three symbol sizes for intensity VI, VII, and VIII. Among the historical events, 1604, 1609, and 1610 indicate those with a refined location and intensity VI. See the caption of Figure 1 for the description of other symbols. The color version of this figure is available only in the electronic edition.

The earthquake sequence started with a small foreshock of M_L 1.6 that occurred at 23:08:14 on 28 October 2022 and was followed about 19 min later by the M_L 3.5 foreshock; then the mainshock of M_L 4.1 occurred 17 s later. Fifty-nine aftershocks followed, and the majority of the events occurred within the first three days. The earthquake sequence consists of three foreshocks, with the largest event being M_L 3.5, the M_L 4.1 mainshock, and 59 small aftershocks (M_L –0.2 to 2.9). Hereafter we call the M_L 3.5 foreshock, the third event in the sequence, the foreshock unless there is confusion. The 33 earthquakes reported by KMA and the additional 30 small aftershocks we detected and located are listed in Table 1. Recently, Sheen *et al.* (2023) reported the detection and location of 25 microearthquakes (M –0.03 to 0.7), in addition to 25 events on the KMA list during the first three days after the mainshock using a template-matching technique, and Song *et al.* (2022) detected a total of 144 small earthquakes in the first 12 days following the mainshocks, and four events were located in addition to the KMA list.

The 28 October 2022 Goesan earthquake occurred in the central part of the southern Korean Peninsula, which is at the eastern margin of the Eurasian plate (Fig. 1). Although the southern part of the peninsula is only about 500 km from the Philippine Sea plate boundary, and much of the peninsula is within about 1000 km from the seismically active Japanese islands, the Korean Peninsula is considered a stable continental region due to its relatively low seismicity, apparent lack of active geologic features, and a substantial distribution of stable Precambrian terrain (Fig. 1).

The shallow earthquakes of $M > 3.5$ that occurred in and around the Korean Peninsula during 1905–2020 are plotted in Figure 1 (see Data and Resources). The earthquake catalogs for the instrumental period (1905–2020) from KMA and the International Seismological Centre (ISC) indicate that four earthquakes with substantial property damage have occurred, but no casualties are known in the Korean Peninsula during the instrumental period. The 3 July 1936 Ssanggyesa earthquake (MMI VIII; M 5.3) caused substantial damage in south-central Korea; an earthquake of magnitude 5.0 (KMA) that occurred near the town of Hongseong on 7 October 1978 caused minor damage; 12 September 2016 M_w 5.5 Gyeongju earthquake caused minor damage; and 15 November 2017 M_w 5.4 Pohang earthquake that is likely induced by enhanced geothermal field incurred major damage probably due to its shallow focal depth (Kim *et al.*, 2018; Lim *et al.*, 2020; Fig. 1).

In this article, we briefly review the geologic setting of the region, in particular, around the epicentral region, and then determine the focal mechanism of the Goesan earthquakes by modeling complete records at local distances (<100 km) in the relatively high-frequency band. We relocate the earthquakes of the sequence to identify the source geometry using a high-resolution waveform cross-correlation (WCC) technique and then estimate source parameters—source radii and stress

drops of the largest earthquakes of the 2022 Goesan sequence to shed light on seismogenesis of the region—Ogcheon fold belt in southern Korean Peninsula.

GEOLOGIC SETTING AND SEISMICITY

The 2022 Goesan earthquake sequence occurred in the central part of the Ogcheon fold belt that runs diagonally across the southern Korean Peninsula in a southwest–northeast trend with a width of 50–60 km (OB in Fig. 1; e.g., Kim and Van der Voo, 1990; Cluzel *et al.*, 1991). The Ogcheon fold belt is the boundary between two Precambrian blocks: Gyeonggi massif (GM) in the north and Yeongnam massif (YM) in the south (Fig. 1). The Ogcheon belt is formed as a result of the collision between the southern and northern Massifs in the late Precambrian to early Paleozoic (Kim and Van der Voo, 1990). Cluzel *et al.* (1991) proposed that nappes in the Ogcheon belt represent intracontinental orogeny involving the opening and subsequent closure of an aborted rift, and that the Ogcheon orogeny was in Late Silurian-Early Devonian. The early Paleozoic volcanosedimentary rocks were folded during the orogeny, and terrigenous sediment was then deposited on top during the Middle Carboniferous.

Geologic formations around the epicentral area predominantly consist of metavolcanic rocks of late Precambrian, and granites intruded in the Jurassic. Rocks were folded and faulted heavily, and showed complex structures (Park, 2005). A pair of faults are mapped close to the epicentral area that runs between towns Eumseong and Mireuk with a trend of east-southeast (ESE)–west-northwest (WNW; Fig. 2; Korea Institute of Geoscience and Mineral Resources [KIGAM], 2019). The closest fault segment that passes through the epicentral area is the Jogok fault (Fig. 2; Park, 2005). The Jogok fault should be called the Jogok fault system, because it may consist of more than one fault plane at depth arranged en echelon (S.-I. Park, personal comm., 2023). The Jogok fault system shows left-lateral motion based on offsets of a Mesozoic dyke formation along the fault trace. Song *et al.* (2022) suggested that the 2022 Goesan earthquake occurred on the Jogok fault at depth. They found fault outcrops along the trace of the Jogok fault system up to about 8.7 km from the epicenter and reported a trace of possible paleoseismic activity along the fault.

Relatively large earthquakes of $M > 4$ have occurred along the northern and southern boundaries of the Ogcheon belt (Figs. 1, 2), and a pair of significant earthquakes occurred in the northeastern part of the belt; Taebaeksan basin—20 January 2007 M_w 4.6 Odaesan earthquake (Kim *et al.*, 2010) and 13 December 1996 M_w 4.7 Yeongwol earthquake (Baag *et al.*, 1998; Figs. 1, 2). The 2022 Goesan earthquake occurred in a seismically quiet area in the central Ogcheon fold belt where there was no known earthquake of magnitude greater than 4 within the 50 km radius from the epicenter. The nearest one occurred on 15 September 1978, about 60 km south of the epicenter, with a reported magnitude of m_b 4.7 (International

TABLE 1
List of 2022 Goesan, Korea, Earthquake Sequence

ID	Date Time (yyyy/mm/dd hh:mm:ss.ss)	Latitude (°N)	Longitude (°E)	Depth (km)	Magnitude		
					M_L^*	$M_w^†$	H Error [‡] (km)
1	2022/10/28 23:08:14.82	36.8797	127.8783	13.1	1.6	1.87	0.16
2	2022/10/28 23:09:32.52	36.8808	127.8758	12.7	1.3	1.23	0.18
3	2022/10/28 23:27:33.55	36.8801	127.8780	12.8	3.5	3.50	0.15
4	2022/10/28 23:27:50.22	36.8772	127.8822	13.1	4.1	3.75	0.18
5	2022/10/28 23:29:09.99	36.8835	127.8662	12.8	2.2	2.52	0.14
6	2022/10/28 23:29:18.81	36.8805	127.8847	12.8	2.9	3.10	0.15
7	2022/10/28 23:31:07.07	36.8767	127.8804	13.0	1.0	0.84	0.22
8	2022/10/28 23:32:09.21	36.8796	127.8768	12.4	1.2	0.62	0.20
9	2022/10/28 23:35:33.81	36.8769	127.8830	12.7	0.9	0.57	0.16
10	2022/10/28 23:39:33.67	36.8784	127.8780	12.8	1.1	0.81	0.17
11	2022/10/28 23:41:16.55	36.8772	127.8835	12.6	1.1	0.58	0.18
12	2022/10/28 23:43:40.51	36.8795	127.8789	12.9	0.9	0.75	0.19
13	2022/10/28 23:46:07.37	36.8761	127.8785	12.9	0.9	0.72	0.27
14	2022/10/29 00:39:29.16	36.8771	127.8836	13.2	1.2	0.70	0.18
15	2022/10/29 00:47:55.32	36.8777	127.8814	12.9	0.9	0.78	0.21
16	2022/10/29 00:54:10.88	36.8785	127.8777	13.4	1.2	0.88	0.19
17	2022/10/29 02:04:00.64	36.8783	127.8791	12.9	1.1	0.75	0.18
18	2022/10/29 07:09:43.19	36.8783	127.8755	12.6	1.3	0.89	0.15
19	2022/10/29 12:10:55.86	36.8779	127.8771	12.9	1.1	0.57	0.20
20	2022/10/29 19:02:27.21	36.8797	127.8784	13.4	1.2	0.48	0.17
21	2022/10/30 15:09:26.92	36.8763	127.8861	12.5	1.2	0.39	0.22
22	2022/10/30 16:37:59.61	36.8794	127.8745	12.5	1.2	0.62	0.14
23	2022/10/31 10:00:23.53	36.8701	127.8821	12.9	0.9	0.66	0.18
24	2022/10/31 11:22:22.60	36.8798	127.8833	12.7	1.3	0.71	0.16
25	2022/10/31 17:27:52.92	36.8806	127.8752	12.5	2.9	3.17	0.10
26	2022/11/01 02:35:16.97	36.8702	127.8854	12.7	0.8	0.79	0.30
27	2022/11/01 15:15:24.56	36.8791	127.8826	12.6	0.9	0.46	0.19
28	2022/11/03 22:07:51.16	36.8775	127.8828	12.9	1.0	0.92	0.19
29	2022/11/07 00:46:50.33	36.8745	127.8789	12.8	1.4	1.51	0.18
30	2022/11/07 00:52:03.80	36.8748	127.8794	12.8	0.7	0.77	0.21
31	2022/11/13 13:21:08.92	36.8772	127.8852	13.2	1.7	1.94	0.24
32	2022/11/16 21:09:41.98	36.8772	127.8760	12.9	0.9	0.77	0.23
33	2023/01/14 16:56:28.28	36.8836	127.8656	12.6	1.6	1.81	0.14
103	2022/10/28 23:32:42.92	36.8747	127.8785	13.0	0.88	0.61	0.27
107	2022/10/29 08:09:30.70	36.8758	127.8792	12.9	0.86	0.58	0.25
111	2022/10/30 23:49:07.34	36.8742	127.8838	12.7	0.42	0.09	1.15
113	2022/11/01 05:40:34.73	36.8791	127.8749	12.5	1.01	0.75	0.27
114	2022/11/03 05:10:41.24	36.8691	127.8897	13.0	0.30	-0.04	0.54
116	2022/11/03 22:33:34.42	36.8799	127.8814	12.9	0.67	0.37	0.45
122	2022/11/06 12:32:14.68	36.8709	127.8769	12.1	0.29	-0.06	0.45
123	2022/11/06 20:50:11.55	36.8786	127.8740	12.7	0.84	0.56	0.18
124	2022/11/08 15:19:57.88	36.8806	127.8679	11.8	0.49	0.17	0.26
125	2022/11/11 17:00:50.65	36.8783	127.8850	12.8	0.31	-0.03	0.17
126	2022/11/12 13:08:38.26	36.8797	127.8781	12.7	-0.20	-0.60	0.46
213	2022/10/28 23:42:28.32	36.8796	127.8692	12.9	0.79	0.50	0.34
215	2022/10/28 23:44:34.76	36.8769	127.8821	12.5	0.96	0.70	0.22
217	2022/10/28 23:49:12.15	36.8739	127.8801	13.1	0.76	0.47	0.33
218	2022/10/28 23:51:25.29	36.8746	127.8798	12.9	0.67	0.37	0.38
219	2022/10/29 00:13:34.43	36.8740	127.8858	13.7	0.71	0.42	0.32
220	2022/10/29 00:28:05.80	36.8782	127.8715	13.1	1.01	0.75	0.59
221	2022/10/29 00:33:43.13	36.8782	127.8764	12.5	0.79	0.50	0.39
224	2022/10/29 00:52:26.27	36.8758	127.8784	12.6	0.86	0.58	0.53
226	2022/10/29 01:04:37.24	36.8787	127.8733	12.2	0.62	0.31	0.23
230	2022/10/29 10:16:06.39	36.8670	127.8759	14.7	0.55	0.24	0.57

(continued)

TABLE 1 (Continued)

ID	Date Time (yyyy/mm/dd hh:mm:ss.ss)	Latitude (°N)	Longitude (°E)	Depth (km)	Magnitude		
					M_L^*	$M_w^†$	H Error‡ (km)
234	2022/10/29 17:00:26.97	36.8754	127.8880	12.8	0.59	0.28	0.30
235	2022/10/29 18:03:51.43	36.8776	127.8751	13.0	0.73	0.44	0.32
237	2022/10/29 19:21:00.20	36.8781	127.8833	13.5	0.65	0.35	0.31
238	2022/10/29 22:17:48.09	36.9018	127.8878	14.2	0.48	0.16	0.55
239	2022/10/30 00:05:45.08	36.8799	127.8908	13.0	0.71	0.42	0.29
240	2022/10/30 00:31:53.45	36.8743	127.8961	12.9	0.80	0.52	0.33
245	2022/10/31 09:11:18.19	36.8885	127.8872	13.5	0.59	0.28	0.56
249	2022/10/31 17:30:16.80	36.8796	127.8751	12.3	0.76	0.47	0.25
250	2022/10/31 20:32:38.29	36.8795	127.8703	11.7	0.57	0.26	0.52

Date, time, latitude, longitude, depth, and H error are from HYPOINVERSE event location.

* M_L (local magnitude) is reported by Korea Meteorological Administration (KMA) for ID 1–33, relative magnitude from amplitude ratios of detected and template events for event ID 103–126, and magnitude given by Sheen et al. (2023) converted to KMA magnitude using a linear regression for ID 213–250.

† M_w is the moment magnitude from the seismic moment from waveform inversion (3, 4, 6, and 25), and from spectral analysis for events ID 1–33 (see Text S3), and converted from M_L using a regression relation $M_w = 1.12 M_L - 0.38$ (see Fig. S11) obtained for 2022 Goesan earthquakes.

‡H error is the crude horizontal location uncertainty at a 95% confidence level.

Seismological Centre [ISC], 2023). The area is known as the Songnisan seismic zone (Lee, 2010; Fig. 2).

To ensure the seismicity for a long time window, we examined the historical earthquake catalog for Korean Peninsula during 2–1904 A.D., which has 2173 events listed (Korea Meteorological Administration [KMA], 2012). In the catalog, there were three events of significance around the epicentral area of the 2022 Goesan earthquake that have origin time and location with some confidence, as plotted in Figure 2. Two earthquakes—13 September 1609 and 9 April 1610—occurred in Boeun County about 45 km south of the Goesan earthquake and were assigned intensity VI (MMI). The epicenters of these two events are the same and are in the aforementioned Songnisan seismic zone (Fig. 2), and the historical registry describes them as the ground-motion traveling from north to south and sounding similar to thunder, residents were shaken, and the motion ceased after an extended period. Two earthquakes had nearly the same reports. An earthquake of intensity VI occurred on 30 July 1604 at midnight near Mungyeong City (Fig. 2). The event registry says that the ground motion traveled from east to west and ceased after

an extended period of time; the additional earthquakes occurred at 2 a.m. and 4 a.m.; and it was an extraordinary event to have three earthquakes in a single day. Other events in the catalog have large location uncertainty being a midpoint of the huge felt report area (~100 km radius) and are plotted with gray circles in Figure 2.

The present-day northeast Japan arc and much of the southern Korean Peninsula are currently under east–west horizontal compression. The recent earthquakes that occurred in the Ogcheon fold belt showed predominantly subhorizontal P axes trending east-northeast (ENE)–east (e.g., Kim et al., 2010), which is consistent with the findings that broad stress fields within plates are consistent with the direction of absolute plate motion (Zoback and Magee, 1991; Fig. 1, inset). Accordingly, we expect the orientation of maximum horizontal stress around the epicentral region and throughout much of the Korean Peninsula to be due east–west.

In the following section, we determine the focal mechanisms of the earthquake sequence, and compare them with the mapped fault traces around the epicentral area in an attempt to correlate the mapped fault and the earthquake sequence.

TABLE 2

Seismic Moment and Focal Mechanism of Four Largest Events from Waveform Moment Tensor Inversion

ID	M_w	Seismic Moment (10^{14} N·m)	Depth (km)*	NP1†		NP2		P axis
				s/d/r (°)	s/d/r (°)	s/d/r (°)	tr/pl (°)	
3	3.50	2.03 (± 1.57)	14.0	106/86/-19	197/71/-176			60/16
4	3.75	4.77 (± 2.98)	13.5	106/83/17	14/73/173			239/7
6	3.10	0.50 (± 0.36)	12.0	108/79/-31	205/60/-167			62/30
25	3.17	0.63 (± 0.46)	15.0	107/72/-22	204/69/-161			65/28

d, dip; pl, plunge; r, rake; s, strike; and tr, trend.

*Depth is determined from the waveform modeling for mechanism inversion.

†NP1 and NP2 are the two nodal planes of the best-fitting double-couple solution of the focal mechanism.

FOCAL MECHANISM FROM LOCAL WAVEFORM INVERSION

We retrieved waveform data of the earthquake sequence from seismographic stations in the distance range from 8 to 442 km in the southern Korean Peninsula. The sensors at those stations consist of 115 broadband, 21 short-period with the natural period of $T_0 = 1$ or 2 s, and 168 accelerometers, and the stations provided spatial coverage with an interstation distance of ~ 15 km, although the stations are not uniformly distributed. The national seismic network, operated mainly by KMA, has been expanding rapidly since 2016 (primarily accelerometers). All accelerometers are operated with $a \pm 0.5g$ full-scale setting and provide adequate quality data even for microearthquake studies.

We modeled the four largest events of the earthquake sequence with $M_L \geq 2.9$ out of 33 reported earthquakes (Table 1). Synthetic waveforms were calculated with the frequency-wavenumber integration method (Bouchon, 1981; Saikia, 1994) with a two-layer crustal model of the southern Korean Peninsula (Kim and Kim, 1983). We inverted the waveform data by allowing a small time shift between the observed and synthetics, and grid searched over double-couple fault parameters, as given in Kim *et al.* (2010). We added P -wave first-motion data to help constrain the focal mechanism.

Modeling the records of the four largest earthquakes with a magnitude range from M_L 2.9 to 4.1 and inverting for the focal mechanism are straightforward tasks; however, due to the unusually close occurrence of those events in time, records are carefully windowed to ensure that proper signals are analyzed for each event as described in the supplemental material, available to this article (Text S1). For example, the foreshock occurred 16.7 s before the mainshock within 0.5 km apart, and, hence, for the foreshock, the observed S waves at stations beyond the epicentral distance of ~ 100 km are not useful for waveform fitting, because the P -wave arrivals from the mainshock interfere. Similarly, for the mainshock, P waves at stations beyond 75 km are contaminated by the S waves from the preceding foreshock (Fig. S1).

For local waveform data ($\Delta < 100$ km) from small earthquakes ($M \leq 3.0$), the frequency band available for successful waveform modeling is limited due to the size of the events, focal depth (shallow events excite more long-period signals), and ambient noise level. Usually signals in the long-period band are preferred, because signals are less affected by lateral variation of crustal structure in the longer period. In the case of Goesan earthquakes, 0.1–2 Hz band might be useful for the analysis. However, due to events occurring close in time (9 s between events 5 and 6; 17 s between 3 and 4), we had to use a higher frequency band to avoid waveform contamination. The used frequency bands are 0.5–2 Hz for event 6, 0.3–1 Hz for events 3 and 25, and 0.08–0.5 Hz for the mainshock.

Focal mechanism parameters obtained from the local waveform inversion are listed in Table 2, and comparisons of

observed and synthetic traces for each event are plotted in Figures S2–S5. The focal depths for each event are constrained by calculating synthetics at various depths, and assigning the depth that produced the least-fitting errors between the observed and synthetic traces (Fig. S6). The focal depth of the modeled events ranges from 12 to 16 km with an estimated uncertainty of ± 2 km (Fig. S6); hence, the events likely have occurred in the deeper part of the upper crust.

The focal mechanisms of the four events suggest that they are predominantly strike-slip events. The nodal plane striking ESE–WNW (106° – 108°) and dipping steeply (72° – 86°) to the southwest (SW) is consistent among the four events. The second nodal plane is also common to all four events and strikes north-northeast (NNE)–south-southwest (SSW) with a steep dip angle of 60° – 73° . However, the rake of the left-lateral nodal planes shows an opposite sign among events, that is, the foreshock and two aftershocks have a rake ranging from -19° to -31° , but the mainshock has 17° for the first nodal plane (Table 2; Fig. 3a). The P axis of all four events trends east-northeast (ENE)–west-southwest (WSW). The plunge of the mainshock P axis is subhorizontal (7°), but the plunge of three events is between 16° and 30° . Nevertheless, an overall focal mechanism is nearly uniform: predominantly near-vertical strike-slip faulting (Table 2).

To assess the state of stress in the Goesan area, we obtained additional focal mechanisms of the five small events using the P -wave first-motion polarities as shown in Figure S7. Nine focal mechanisms are inverted for the local stress tensor by two methods (Michael, 1984; Gephart, 1990). Using the method of Gephart (1990), the best-fitting stress model has an average misfit value of 2° and a corresponding stress ratio $R = (\sigma_1 - \sigma_2)/(\sigma_1 - \sigma_3) = 0.35$ (Fig. S8b). Whereas the stress field is linearly inverted using the method of Michael (1984) with noise realization (Fig. S8c).

The two stress inversion methods yield consistent values for stress axes, and we take an arithmetic mean of two solutions. The greatest principal stress axis σ_1 trends WSW ($253^\circ \pm 8^\circ$) and plunges with a moderate angle ($20^\circ \pm 1^\circ$), and σ_3 trends north-northwest ($345^\circ \pm 2^\circ$) and plunges subhorizontal ($6^\circ \pm 16^\circ$). The orientation of the stress axes is broadly consistent with an average value in the southern Korean Peninsula. The plunge of σ_1 is slightly steeper than the reported average value ($\sim 10^\circ$) over the Korean Peninsula, whereas the trend is comparable to the average value of $\sim 70^\circ$ (e.g., Soh *et al.*, 2018). The stress axes orientation suggests that the 2022 Goesan earthquake epicentral region may accommodate oblique faulting motion in a predominantly strike-slip regime.

LOCATION OF THE 2022 GOESAN EARTHQUAKE SEQUENCE

We located 33 earthquakes initially reported by KMA using P and S arrival-time picks at about 20 stations within ~ 80 km distance using HYPOINVERSE (Klein, 1978). We located events

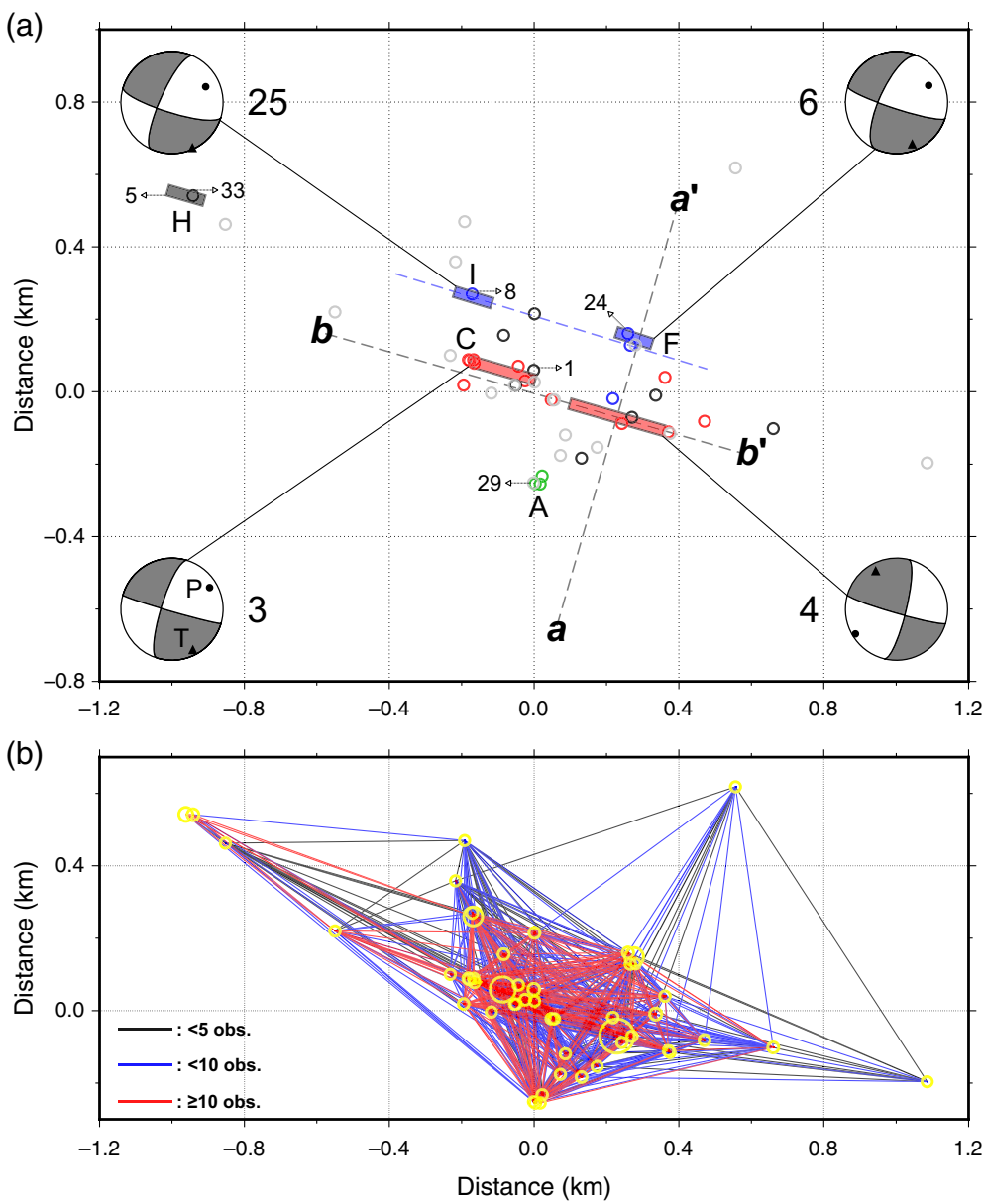


Figure 3. Double-difference (dd) earthquake relocation. (a) Map view of DD locations using the phase and cross-correlated data. Fifty-one events are clustered and relocated, whereas 12 events are not relocated. Five larger events are plotted by thick lines whose length is scaled to the source radius, and smaller events are plotted by circles. Circles and thick lines are color coded as; red represents events aligned along the mainshock fault; blue represents two largest aftershocks 6, 25, and their clustered events (clusters F and I); green represents aftershock 29 and events in cluster A; and black represents events not correlated with other events. Dashed lines indicate the strike of nodal planes of the mainshock and event 6. Focal mechanisms of the four largest events are plotted on a stereographic projection (lower hemisphere). (b) Connectivity plot of the 1786 event pairs of 51 relocated events at the final relocation iteration. It consists of 840 links from correlation data with cross-correlation coefficient (C_c) ≥ 0.9 and 946 event link pairs from catalog phase data. The event pairs linked are color coded to indicate how many station observations are in each event pair: red ≥ 10 , blue ≥ 5 , and black < 5 observations. The color version of this figure is available only in the electronic edition.

using a velocity model for the southern Korean Peninsula as used for the waveform modeling (Kim and Kim, 1983). Events are located with small location uncertainty because of an adequate station azimuthal coverage with the maximum gap of less than 90° (see Fig. 2). The average horizontal and vertical

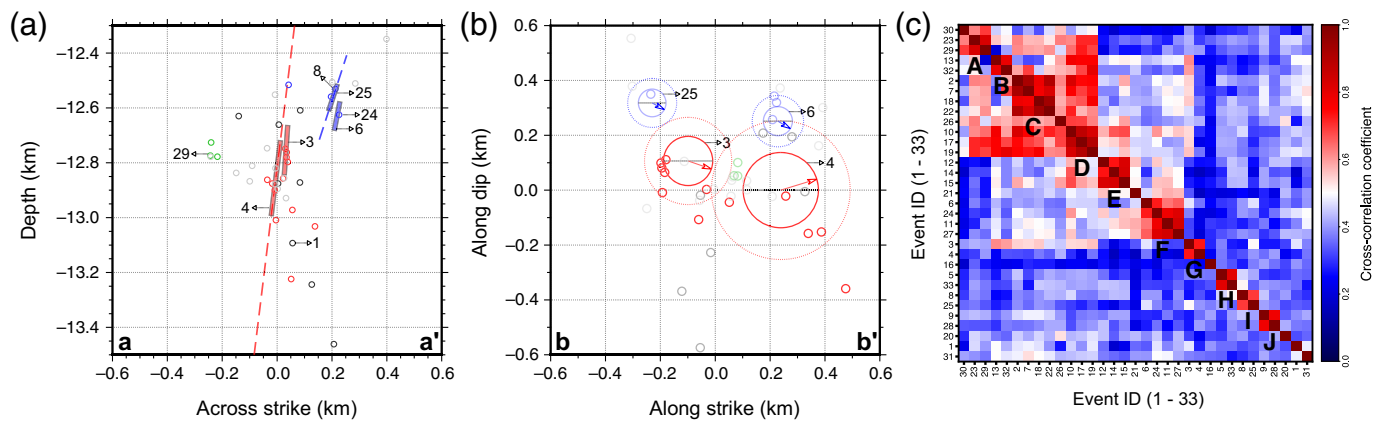
location errors are 0.44 ± 0.09 and 0.84 ± 0.14 km (95% confidence level), respectively, for 33 events. The focal depths are fairly well constrained, because the nearest station CHJ3 is situated about 8.5 km, which is less than the average focal depth of ~ 13 km.

The foreshock serves as a reference event in the sequence, because the event has the best quality P and S arrival-time pick data among the events. The mainshock occurred 16.7 s after the foreshock; and, hence, its P arrivals at stations beyond ~ 80 km could not be used because the P arrivals were contaminated by the S wave and its coda of the preceding foreshock. Although horizontal and vertical location errors are small (< 0.8 km), events are distributed broadly and without showing any alignment (Fig. 3a).

In addition to 33 reported events, we detected and located 30 additional small earthquakes in the sequence. These 30 small earthquakes were detected starting about 5 min after the mainshock and for about two weeks, and had a local magnitude range from -0.2 to 1.01 . These detected earthquakes are located using the same method as the initial 33 events, and they cluster around the mainshock (Fig. S9a). A total of 63 earthquakes located individually are listed in Table 1 and plotted in Figure S9a. The average horizontal and vertical location errors increase to 0.68 km and 0.93 km (95% confidence level), respectively, when we evaluate errors for all 63 events location.

Precise relocation of the earthquake sequence using the double-difference method

We relocated all the 63 earthquakes in the sequence by employing the double-difference (DD) earthquake relocation method



using the computer code hypoDD (Waldhauser and Ellsworth, 2000; Waldhauser, 2001). We first relocated the events using the P - and S -wave differential travel times of event pairs derived from the phase data. We clustered events with the maximum interevent separation distance of 1 km and derived 10,066 differential times from phase data on 1157 event pairs. Each event pair has an average of nine P - or S -wave observations. The connectedness of event pairs used for DD relocation using only the phase data is shown in Figure S10. Most of the 60 relocated events using only differential times derived from phase data are aligned along the ESE–WNW, which is consistent with the nodal plane striking 106° of the mainshock focal mechanism (Fig. S9b). However, the events aligned with a width of ~0.6 km along the alignment (Fig. S9b), which seems too wide for the M_w 3.8 earthquake sequence.

Hence, we refined the DD relocation by adding differential times of the event pairs derived from WCC of the P and S waves. The WCC technique reduces the arrival-time picking errors (e.g., Schaff *et al.*, 2004). We filtered P - and S -wave data in a 2–25 Hz band, and retained measurements with the cross-correlation coefficient (Cc) greater than 0.9 for both P and S phases. We obtained 3901 P - and S -wave differential travel times from the 1469 event pairs using the WCC technique. We have about three observations per event pair.

The relocation result using differential travel times from both the phase and WCC shows that most earthquakes are

Figure 4. (a) Across-strike cross section of the DD locations along (a–a'). Red and blue dashed lines indicate the fault plane of the mainshock and events 6 and 25, respectively. Other notations used are the same as in Figure 3a. A total of 51 relocated events are plotted. (b) Fault-plane view of the earthquake sequence. Circles represent the events and are plotted by their scaled source radius. Dotted circles indicate radii expected from the Brune source model. Red and blue arrows indicate the rake angle for each event. (c) Cc matrix of initial 33 events reordered according to the hierarchical clustering. Each column and row represents an earthquake for which ID is given subsequently (Table 1). Subclusters of two or more events are labeled A–J, and six events (events 1, 16, 20, 21, 26, and 31) are not correlated to other events. The color version of this figure is available only in the electronic edition.

now located close together and aligned along a pair of lineaments with small location errors as shown in Figure 3a. The mean horizontal and vertical location errors estimated via the bootstrap method are 0.035 km and 0.026 km, respectively, in the 95% confidence level. The events can be grouped into three distinct clusters. The first cluster consists of all the foreshocks (events 1–3) and the mainshock (event 4), together with a number of aftershocks, align along the ESE–WNW direction (red dashed line in Fig. 3a). The cluster forms a plane with a strike direction consistent with the nodal plane of the mainshock focal mechanism (Fig. S3).

The second cluster includes the two large aftershocks (M_L 2.9; events 6 and 25) with related aftershocks, and the events align along the ESE–WNW direction (blue dashed line in Figs. 3a,

TABLE 3
Source Parameters of the 2022 Goesan Earthquake Sequence from Empirical Green's Function (EGF) Analysis

Event Number	Event Pairs*	Distance Range (km)	f_c (Hz)	r_0 (km)	$\Delta\sigma$ (MPa)	$\Delta\sigma_B$ (MPa)
3	1, 4, 6, 25	8.5–99.8	8.08 ± 0.36	0.094	106.6	19.2
4	1, 3, 6, 25	8.5–99.8	5.59 ± 0.83	0.135	83.7	15.1
5	33	8.5–44.0	$14.40 \pm 1.09^\dagger$	0.053	20.4	3.7
6	1, 3, 24	8.5–49.0	14.58 ± 0.74	0.052	157.3	28.3
25	1, 3, 4, 8	8.5–99.8	14.04 ± 1.21	0.054	178.9	32.2

f_c , corner frequency with its standard deviation; r_0 , source radius calculated from the circular fault model of Madariaga (1976); $\Delta\sigma$, stress drop calculated with source radius assuming the model of Madariaga (1976); and $\Delta\sigma_B$, stress drop calculated from source radius assuming the source model of Brune (1970, 1971).

*Paired as main-EGF or EGF-main with the event given in column 1 and event IDs in Table 1.

†Standard deviation is given as $(f_{max} - f_{min})/2$, because only a single pair was used to obtain the estimate.

4a). The focal mechanisms of events 6 and 25 are nearly identical and share common nodal planes. These events have a similar strike and dip direction with the mainshock fault plane, but their locations are ~0.2 km northeast off from the mainshock fault plane (Figs. 3a, 4a). The two events likely lie on a fault plane parallel to the mainshock fault plane (Figs. 3a, 4a). A cluster of three small-magnitude events (events 23, 29, and 30) forms the third cluster, and they are located ~0.3 km SW of the mainshock fault (green circles in Fig. 3a). However, the cluster consists of only three events with very small magnitudes (the largest event 29 is M_L 1.4); no further analysis was possible.

The relocation result shown in Figure 3 indicates that the 0.8 km long lineament striking ESE–WNW that encompasses the majority of events, including the foreshock and the mainshock, is consistent with the nodal plane of the mainshock focal mechanism striking 106°. This plane is likely the main fault plane of the 2022 Goesan earthquake sequence. We examined the interconnectedness of 51 relocated earthquakes using a connectivity plot for 1786 event link pairs derived from the 946 catalog and 840 correlation data used in the final iteration (Fig. 3b). The connections between earthquakes in Figure 3b suggest that many of these events could be relocated with correlation data alone.

Hierarchical cluster analysis of the earthquake sequence

The precise relocation of the sequence revealed three groups of events. Events in each group should show similar waveforms and help to characterize the earthquake sequence further. We cross correlated S waves from 33 events recorded at station CGAA ($\Delta = 23.5$ km, AZ = 216°; Fig. 2) and performed hierarchical clustering analysis. The S waves in a 1.5 s window on horizontal components are cross correlated after applying the 1–30 Hz bandpass filter. The reordered Cc matrix is plotted in Figure 4c.

The Cc matrix shows five distinct subclusters with more than three events and five doublets (Fig. 4c). Six events are not associated with other events. The clusters C–E, as well as doublets B, G, and J, form a cluster that contains 16 events, with the foreshock and mainshock corresponding to the events on the main fault plane identified from the relocation (Figs. 3a, 4a; red circles).

The cluster F (events 6, 11, 24, and 27) and doublet I (events 8 and 25) represent fault patches subparallel to the main fault (blue circles in Figs. 3a, 4a). Events 5 and 33 are located about 1.0 km further west of the mainshock (Fig. 3a), and form a doublet based on their waveform similarity (Fig. 4c, doublet H). The cluster analysis using the Cc matrix revealed two distinct clusters on the main and subparallel faults—an isolated cluster (A) and a doublet (H)—and supports the results of the event relocation.

SOURCE PARAMETERS: CORNER FREQUENCY AND STRESS DROP

We determined corner frequencies of the five largest events with $M_L \geq 2.2$ (events 3, 4, 5, 6, and 25) by the empirical Green's

function (EGF) approach in the spectral domain. The S-wave spectra of the large target events are divided with that of the collocated small EGF event to retrieve source spectra by eliminating the path and site effects. We selected the target main event and EGF pair that satisfy the basic requirements for a stable EGF analysis as the pair should be collocated, have nearly the same focal mechanism, and must have the amplitude ratio of at least a factor of 5 (i.e., $\Delta M \geq 0.7$). To ensure the reliability of corner frequency measurements for the five largest events, we employed multiple main-EGF pairs for each event. To overcome the paucity of EGF events, we also constrained the corner frequency by utilizing the large-event corner frequency (f_{c1}) and the small-event corner frequency (f_{c2} ; Text S2). For example, event pairs 4–6 and 3–6 are used to constrain the corner frequencies of events 3, 4, and 6. EGF event 1 (M_L 1.6) is selected for all the four target main events, except event 5. Event 24 (M_L 1.3) is selected as EGF for event 6 (M_L 2.9; cluster F). All the utilized event pairs are listed in Table 3.

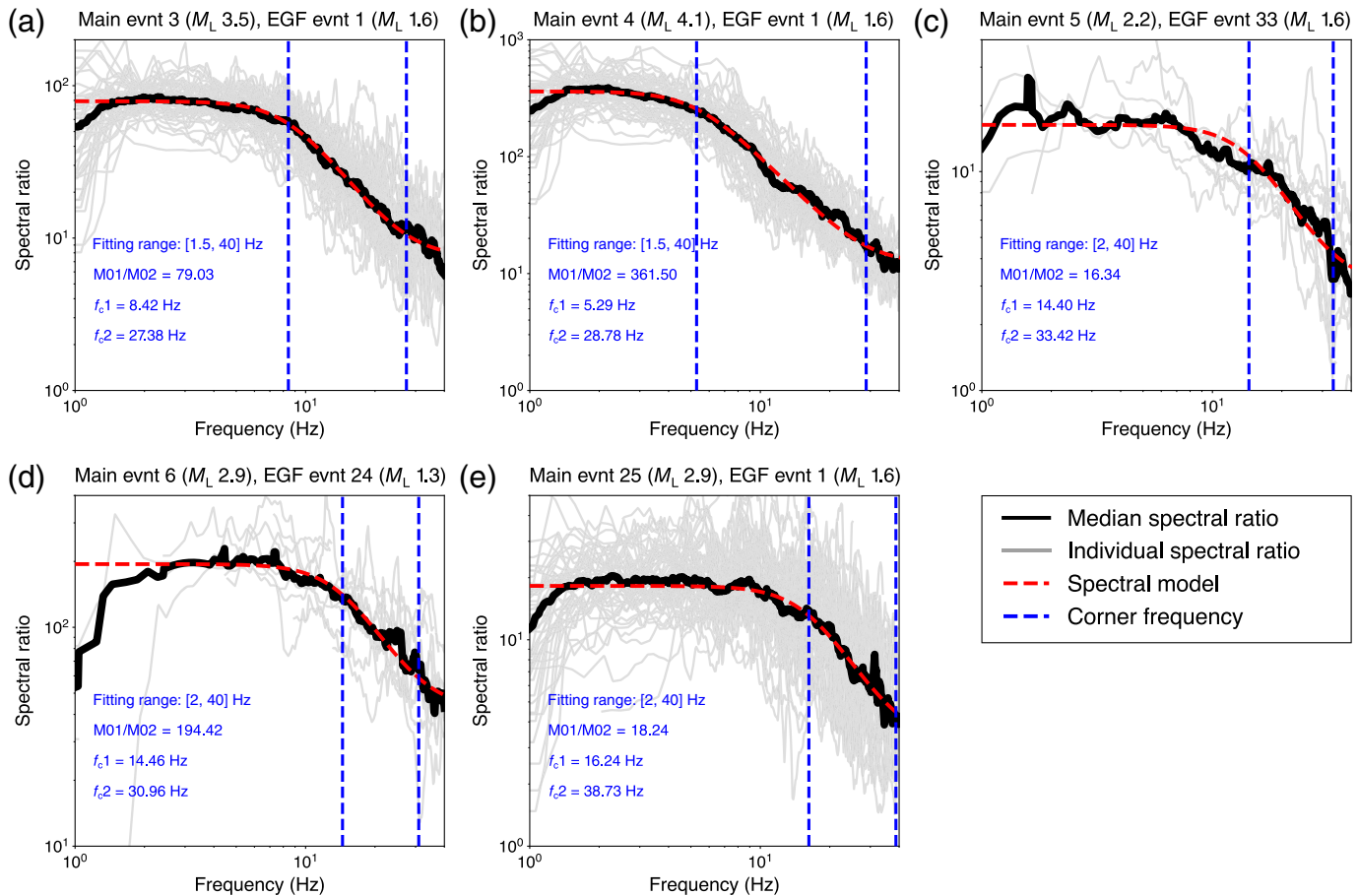
We calculated the spectra of the S waves on the transverse component using a variable time window length at each station scaled for distance as (distance/25 + 1) s and multitapered the signal (e.g., Prieto, 2022). Waveform data from the earthquake sequence have a fairly good azimuthal coverage despite a limited distance range due to phase corruption from events occurring close in time (Fig. 2, and Fig. S1). Preliminary analysis of seismic records from the mainshock at the local distances showed no obvious azimuthal dependence of S-wave signals. Hence, we stacked the spectral ratios obtained for each station by taking the median ratio at each discrete frequency, and only the spectral ratios at frequencies with signal-to-noise ratio (SNR) ≥ 2 are stacked (e.g., Abercrombie, 2015; Daniels *et al.*, 2019).

The stacked spectral ratio $U(f)$ for the five main and EGF event pairs is plotted in Figure 5, and additional stacked spectral ratios are shown in Figure S11. We assumed the ω -square source model (Aki, 1967), and we grid searched for the moment ratio and corner frequencies of the main and EGF events that minimize the variance between the stacked spectral ratio and model spectrum as given in the following equation (e.g., Abercrombie, 2015):

$$U(f) \approx (M_{01}/M_{02}) \times [\{1 + (f/f_{c2})^{2\gamma}\} / \{1 + (f/f_{c1})^{2\gamma}\}]^{1/\gamma}, \quad (1)$$

in which subscript 1 denotes the main event, and 2 denotes the EGF event, respectively, f is the frequency, f_c is the corner frequency, M_0 is the seismic moments, and γ is the constant controlling the shape of the corner frequency. We assumed the high-frequency fall-off with a slope of 2 and selected the constant ($\gamma = 2$) in equation (1) that yields the best fit to the observed ratio (compare with $\gamma = 1$ for Brune, 1970, 1971 and $\gamma = 2$ for Boatwright, 1980 parametrizations).

The corner frequency estimate for the five earthquakes ranges from 5.6 to 14.6 Hz and is given in Table 3. The



uncertainties in the corner frequency estimates are given as standard deviation of the set of corner frequencies from event pairs (Table 3). For the spectral ratio of each EGF pair, uncertainty is calculated by finding the minimum and the maximum corner frequencies ($f_{c\min}$ and $f_{c\max}$) such that the variance does not exceed 1.05 times the minimum variance. If the low-frequency plateau is not well defined, the shape of the misfit curve can be asymmetric; and the best-fit corner frequency may not lie in the middle of the minimum and the maximum corner frequencies (e.g., Viegas *et al.*, 2010; Fig. 5).

We calculated the source radius (r_0) using the relation, $r_0 = k\beta/f_c$, in which β is the shear-wave velocity at the source, f_c is the event corner frequency, and k is the model-dependent constant that relates corner frequency to source radius. For the S wave, the constant k is 0.21 for the circular fault model of Madariaga (1976) and 0.37 for the model of Brune (1970, 1971). We used $\beta = 3.6$ km/s and choose Madariaga's model with $k = 0.21$ to calculate the source radii. The source radius of the foreshock (event 3) is 0.16 km, and the mainshock (event 4) is 0.24 km using source parametrization of Brune (1970, 1971), and presumed rupture areas of the two events overlap slightly; and they would encompass nearly all aftershocks on the main-shock fault plane (Fig. 4b). During the earthquake faulting, it is unlikely to have nearly all aftershocks occur on already ruptured mainshock and foreshock rupture areas. Hence, small

Figure 5. Stacked S-wave spectral ratios from the empirical Green's function (EGF) analysis and best-fitting model for the five largest events in the 2022 Goesan earthquake sequence. (a) M_L 3.5 foreshock, 3–1 pair; (b) mainshock, 4–1 pair; (c) event, 5–33 pair; (d) aftershock, 6–24 pair; and (e) aftershock, 25–1 pair. The event ID and local magnitudes of the main and EGF events are indicated atop each panel. In each panel, individual station spectral ratios are plotted as the light gray curves in the background, the stacked median spectral ratio is plotted as the thick black curve, and the best-fitting theoretical spectral ratio is plotted as the red dashed curves. The spectral model of Boatwright (1980) was used for fitting. Corner frequencies f_{c1} for the main event and f_{c2} for the EGF event are denoted with the vertical blue dashed lines if they are resolved within 80% of the Nyquist frequency (i.e., 40 Hz). The color version of this figure is available only in the electronic edition.

source radii expected from the source model of Madariaga (1976) yield reasonably good mainshock and aftershock distribution on the main fault plane as shown in Figure 4b.

The stress drops ($\Delta\sigma$) are calculated using the seismic moment and source radius, and using the relation, $\Delta\sigma = 7/16 \times M_0/r_0^3$ (Eshelby, 1957). Seismic moment is obtained from the local waveform inversion for events 3, 4, 6, and 25 (see the Focal Mechanism from Local Waveform Inversion section) and also from spectral analysis of S-wave signal for other events (Table 1, Text S3, Fig. S12). The source parameters, corner frequency, source radius, and stress drop, determined are listed in Table 3. We note that the events on

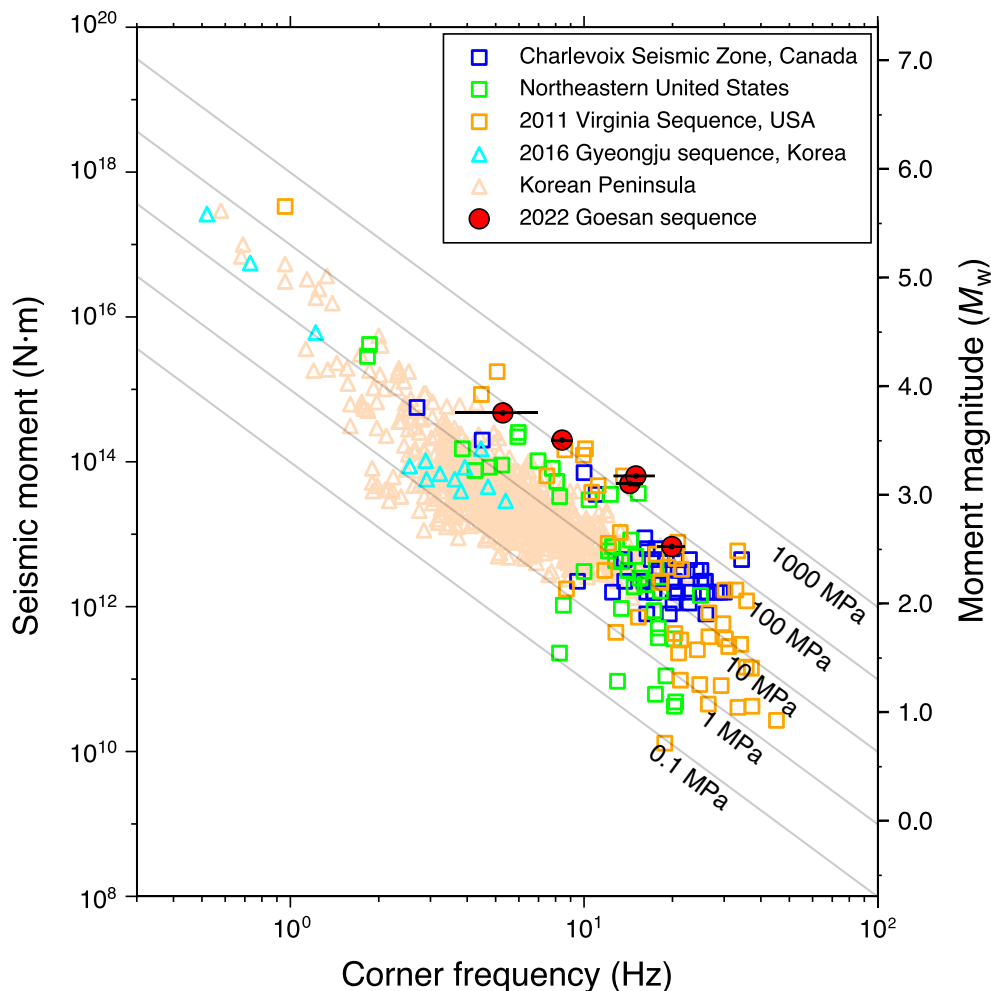


Figure 6. Compiled corner frequency versus seismic moment ($N \cdot m$) from shallow intraplate earthquakes that occurred in the Korean Peninsula (triangles), Eastern North America (ENA; squares), and the five largest events of the 2022 Goesan earthquake sequence analyzed in this study (filled red circles) are plotted. Error bar denoting uncertainty range is plotted by line in the filled red circles. Diagonal lines of constant stress drops are based on the source radius assuming circular fault model of Madariaga (1976) with an S-wave velocity of 3.6 km/s. Data points plotted are from Onwuemeke *et al.* (2018), Shi *et al.* (1998), and Wu and Chapman (2017) for ENA, as well as Chai *et al.* (2020) and Rhee and Sheen (2016) for the Korean Peninsula. The color version of this figure is available only in the electronic edition.

the main fault area, the foreshock, and mainshock, as well as the aftershocks (events 6 and 25) on nearby fault patches, exhibit high stress drops of 83.7–178.9 MPa, whereas event 5, which is located outside of the main fault area, shows 20.4 MPa (Table 3).

DISCUSSION

High stress drops of the 2022 Goesan earthquake sequence

The median value of stress drop is 106.6 MPa from five events (20.4–178.9 MPa; Table 3). The two largest events—foreshock and mainshock—that occurred on the main fault plane showed an average value of 95.2 MPa, and aftershocks (events 6 and 25) that occurred on the adjacent fault patches had an average value of 168.1 MPa. The stress-drop values for these events with

M_w 3.1–3.8 are substantially higher than the values published for the recent earthquakes of comparable size in the Korean Peninsula. Rhee and Sheen (2016) reported stress drops of 0.3–88.9 MPa for 651 events with M_w 2.1–5.3 in southern Korea, and Chai *et al.* (2020) reported stress drops of 0.7–38.1 MPa for events with M_w 2.94–5.58 for 2016 Gyeongju earthquake sequence in southeastern Korea. We convert the stress-drop values from studies assuming the model of Brune (1970, 1971) by multiplying the constant factor ~ 5.56 for comparison with ours—stress drop of Madariaga (1976).

The stress drops reported in various studies are difficult to compare directly because of the different methods used to calculate the corner frequency or source radius (e.g., Wu *et al.*, 2018; Pennington *et al.*, 2021). We compiled corner frequencies from the previous studies on shallow intraplate earthquakes in Korean Peninsula and eastern North America (ENA), and plotted them on the corner frequency versus seismic moment for comparison (Fig. 6). In the plot, stress drops are represented by diagonal lines of constant stress drop, assuming the circular

fault model of Madariaga (1976) with an S-wave velocity of 3.6 km/s. We plotted the ENA results, including Shi *et al.* (1998) study of 41 earthquakes in the eastern United States (0.06–133.4 MPa), Wu and Chapman (2017) for the 2011 Mineral, Virginia, earthquakes (0.1–305.2 MPa), and Onwuemeke *et al.* (2018) study of 518 events in Charlevoix, Canada (2.2–202.3 MPa).

The relatively high stress drops of the 2022 Goesan earthquakes with $M_w > 3$ may represent the high frictional strength of the fault due to the long quiescent period between the ruptures compared with the regions with higher seismicity rates, such as the 2016 Gyeongju earthquake sequence (e.g., Viegas *et al.*, 2010). We note that mostly shallow, induced earthquakes since 2011 in Oklahoma in the central United States show

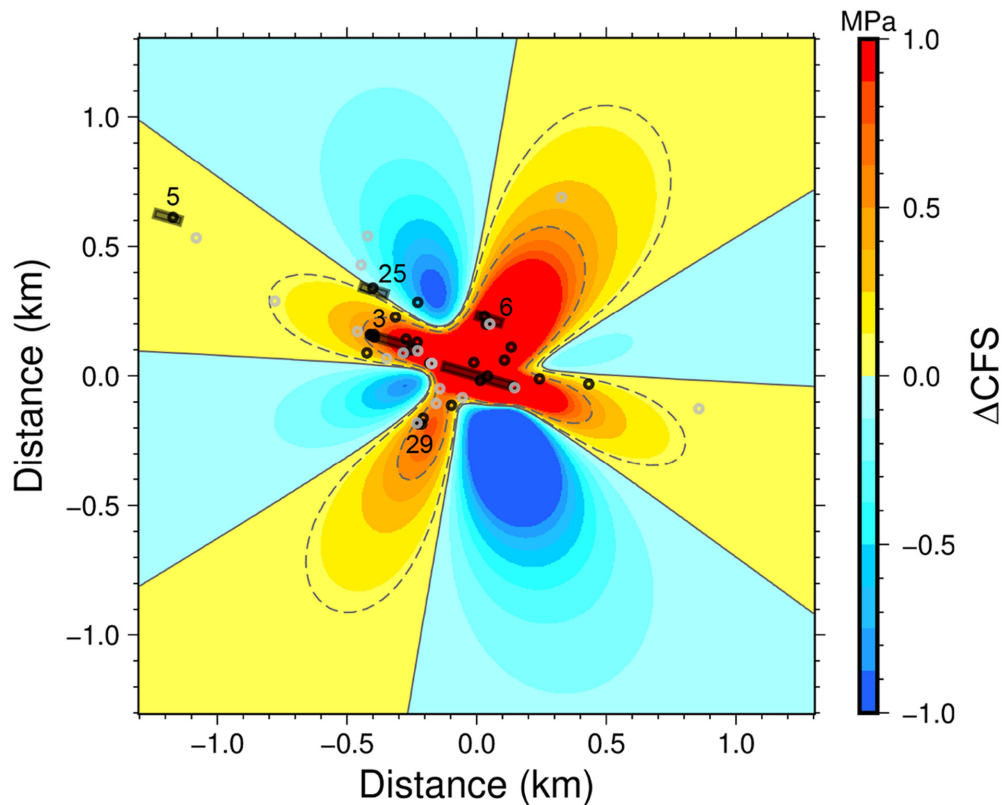


Figure 7. Map view of Coulomb stress changes (ΔCFS) calculated for the mainshock with event 6 as the receiver fault. Red area represents increases in Coulomb stress (stress trigger zone), and the blue area represents decreases in Coulomb stress (stress shadow). Positive Coulomb stress changes are contoured as thin lines = 0 MPa, and dashed lines represent contours of 0.5 and 0.1 MPa. Thirty-three earthquakes are plotted with circles whose sizes are scaled with magnitude, and foreshocks are plotted with green circles. Events 3, 4, 5, 6, and 25 are denoted by their event IDs and are plotted with bars whose lengths are scaled source radii. Coulomb stress rose by 2.1 MPa at event 6 and 2.9 MPa at event 29 locations, whereas the stress rose by 0.2 MPa at event 25 when calculated with event 25 as receiver fault. The mainshock fault is the thick solid line on the center and is modeled as a $0.28 \text{ km} \times 0.22 \text{ km}$ rectangular fault and left-lateral slip motion with a moment of $4.77 \times 10^{14} \text{ N} \cdot \text{m}$ (Table 2). Coulomb stress is calculated for the receiver depth of 12.8 km, and an average frictional coefficient of 0.8 is used. The color version of this figure is available only in the electronic edition.

comparable high stress drops in a similar intraplate region setting (e.g., Wu *et al.*, 2018). It is also suggested as the cases of near-complete stress release that may have contributed to high stress drops in conjunction with long healing times and low-strain rates in an intraplate setting (e.g., Mcclaskey *et al.*, 2012; Im *et al.*, 2017), although near-complete stress drops have also been reported in active faulting areas as for the 2016 M_w 5.2 Borrego Springs earthquake in California (Ross *et al.*, 2017).

Spatiotemporal evolution and interevent triggering of the earthquake sequence

The Goesan earthquake sequence rapidly progressed temporally following the mainshock, and the first 13 events occurred within the first hour (see Table 1 and Fig. S13). The moment release of the whole earthquake sequence is also concentrated in the first hour mostly by the two events—the foreshock and mainshock, even though the sequence lasted about 78 days. (Fig. S13). The

whole sequence, except events 5 and 33 (doublet H), is confined within an ellipsoid of $\approx 0.20 \text{ km}^3$ (principal semiaxes; $a = 0.45 \text{ km}$, along strike direction, $b = 0.375 \text{ km}$, depth direction, $c = 0.25 \text{ km}$, perpendicular to strike).

The spatial distribution of the events in the Goesan earthquake sequence, as revealed by the precise relocation of events and by the waveform similarity analysis as shown in Figures 3 and 4, raises some questions about the drivers behind the spatiotemporal evolution of the M_w 3.8 earthquake sequence.

In particular, the immediate aftershock—event 6 (M_w 3.1) appears to have occurred off the main fault plane about $\sim 0.2 \text{ km}$ to the north (clusters F and I; see Figs. 3, 4). The event distribution does not appear to be a stepover strike-slip faulting (though events have the common strike-slip focal mechanisms), rather they must be triggered by static stress on separate fault (e.g., Helmstetter *et al.*, 2005). Aftershocks are often triggered by static-stress changes caused by a mainshock, and the static stress can trigger

earthquakes over a variety of spatial and temporal scales (e.g., Fan and Shearer, 2016). To assess the interaction between the earthquake faults through the static stress triggering, we examined the Coulomb stress changes during the sequence (Table 2; Fig. 3). The analysis is based on the Coulomb failure criterion that earthquakes can be triggered by the Coulomb stress for which it rose by more than 0.05 MPa on optimally orientated faults (King *et al.*, 1994). We calculated the Coulomb failure stress change (ΔCFS) of the earthquake sequence using a frictional coefficient of 0.8 (Toda *et al.*, 2011; see Data and Resources). More details about the calculation and results are given Text S4. The calculation of ΔCFS for the foreshock indicates that the foreshock likely triggered the mainshock because the static Coulomb stress rose by 0.6 MPa at the mainshock location $\sim 0.3 \text{ km}$ to the ESE (Fig. S14a).

The ΔCFS calculated for the mainshock with event 6 as the receiver fault is shown in Figure 7. The calculation indicates that the mainshock increased the static stress at the event 6

location by \sim 2.1 MPa, which should be sufficient to trigger the event (Fig. 7). It appears to be a triggering of an event on the adjacent subparallel fault, not on the same fault plane (Fig. 3a). Event 29 (M_L 1.4) that is located \sim 0.3 km SSW of the mainshock must also be triggered by the mainshock, because the static stress is raised by \sim 2.9 MPa at the event location (Fig. 7). The event itself is in a cluster of three events—cluster A (Fig. 4c).

Event 25 is the largest aftershock (M_w 3.2) that is likely triggered by the mainshock, because the Coulomb stress rose by 0.2 MPa at the event 25 location when the Δ CFS is calculated with event 25 as the receiver fault (Fig. S14c). Events 25 and 6 are aligned subparallel to the mainshock fault-plane direction. We suggest that they may be two separate strong fault patches (asperities) broken on the subparallel fault plane and surrounded by unbroken barriers (e.g., Aki, 1984). As such, each event ruptured with a common focal mechanism and high stress drops of over \sim 157 MPa (Table 3; Fig. 5).

CONCLUSIONS

The 2022 M_w 3.8 Goesan earthquake sequence occurred in relatively quiet region of the Ogcheon fold belt in central Korea, the sequence progressed rapidly temporally and to a complex spatial extent through interevent triggering, yet the whole sequence happened in a small source volume. We delineated the fault plane of the earthquake sequence based on the precise relocation of the earthquake sequence that revealed a 0.8 km long rupture plane striking ESE–WNW. The fault plane encompasses the majority of events, including the foreshock and the mainshock, and the geometry of the plane is consistent with the left-lateral strike-slip faulting on the ESE-striking nodal plane of the mainshock focal mechanism. The Jogok fault system recently mapped in the region runs through the epicenter with a consistent strike with the main fault plane, and we argue that it is the likely causative fault of the Goesan earthquake sequence.

Events in the main fault plane are triggered by the mainshock, as well as events on adjacent fault patches seemed to be triggered by the mainshock. Δ CFS by the mainshock suggests that the static stress rose to trigger the off-main fault events. Events in the Goesan earthquake sequence appear to be high stress drop events compared with other shallow intraplate earthquakes in Korean Peninsula and may suggest the high frictional strength of the fault due to the long quiescent period in the epicentral region. The local stress field around the Goesan region situated in the central Ogcheon fold belt in the southern Korean Peninsula is a predominantly near-vertical strike-slip faulting regime under subhorizontal compressional stress trending WSW (245°) with a moderate plunge of \sim 20°.

DATA AND RESOURCES

Waveform data of broadband, accelerometer, and short-period seismometers of the Korea Meteorological Administration (KMA) were

downloaded from the National Earthquake Comprehensive Information System website (<https://necis.kma.go.kr>) upon approval. Waveform data from open stations of KMA (network code: KS) and Korea Institute of Geoscience and Mineral Resources (KIGAM; network code: KG) were obtained from the Incorporated Research Institutions for Seismology Data Management Center (IRIS-DMC; http://ds.iris.edu/SeismiQuery/by_network.html); nonopen stations of KMA and KIGAM networks were acquired through written requests. Earthquake catalogs of the 2022 Goesan earthquake sequence and past seismicity (1905–2020) in Korea were accessed from KMA online catalog (<https://www.weather.go.kr/w/ejk-vol/search/korea.do>) and International Seismological Centre (ISC) online bulletin (doi: [10.31905/D808B830](https://doi.org/10.31905/D808B830); <http://isc.ac.uk/iscbulletin/search/catalogue/>). Locations of faults and geologic units in Korea (plotted in Figs. 1, 2) were acquired from Geo Big Data Open Platform (<https://data.kigam.re.kr>). Geologic maps with faults can be accessed online at https://data.kigam.re.kr/mgeo/map/main.do?process=geology_250k, 1:250000 Andong sheet. We used Seismic Analysis Code (SAC; <https://ds.iris.edu/ds/nodes/dmc/software/downloads/sac/>), ObsPy (<https://docs.obspy.org>), Generic Mapping Tools (GMT; v.6.4.0.; <https://www.generic-mapping-tools.org>), Python library Multitaper (<https://github.com/gaprieto/multitaper/>), and Coulomb 3.3 software (<https://temblor.net/coulomb/>). Earthquakes are individually located using the computer code HYPOINVERSE (<https://www.usgs.gov/software/hypoinverse-earthquake-location>). Earthquakes are relocated using the computer code hypoDD (<https://www.ledo.columbia.edu/~felixw/hypoDD.html>). All websites were last accessed in March 2023. The supplemental material includes descriptions of (1) waveform data for modeling and focal mechanisms of the four largest events of the sequence, (2) corner frequency estimation, (3) moment magnitude estimation, and (4) Δ CFS. The document also contains 14 figures that supplement the results presented in the article.

DECLARATION OF COMPETING INTERESTS

The authors acknowledge that there are no conflicts of interest recorded.

ACKNOWLEDGMENTS

The authors appreciate Seung-Ik Park of Kyungpook National University for a helpful discussion about the seismogenic fault of the 2022 Goesan earthquakes. The authors thank editor and associate editor's support to this work, and appreciate Colin Pennington and one anonymous reviewer for their thoughtful comments and constructive reviews. This work was supported by Brain Pool Program through the National Research Foundation of Korea (NRF), funded by the Ministry of Science and Information & Communication Technology (ICT) (2020H1D3A2A02047949). The authors also acknowledge funding from NRF grants by the Korean government (Grant Numbers 2022R1A2C1003006 and 2022R1A5A1085103).

REFERENCES

- Abercrombie, R. E. (2015). Investigating uncertainties in empirical Green's function analysis of earthquake source parameters, *J. Geophys. Res.* **120**, no. 6, 4263–4277, doi: [10.1002/2015JB011984](https://doi.org/10.1002/2015JB011984).
- Aki, K. (1967). Scaling law of seismic spectrum, *J. Geophys. Res.* **72**, 1217–1231, doi: [10.1029/JZ072i004p01217](https://doi.org/10.1029/JZ072i004p01217).

- Aki, K. (1984). Asperities, barriers, characteristic earthquakes and strong motion prediction, *J. Geophys. Res.* **89**, no. B7, 5867–5872, doi: [10.1029/JB089iB07p05867](https://doi.org/10.1029/JB089iB07p05867).
- Baag, C.-E., J. S. Shin, H. C. Chi, I.-B. Kang, and Y.-G. Ryoo (1998). Fault-plane solutions of the December 13, 1996, Yeongweol earthquake, *J. Korean Geophys. Soc.* **1**, no. 1, 23–30.
- Bird, P. (2003). An updated digital model of plate boundaries, *Geochem. Geophys. Geosys.* **4**, no. 3, doi: [10.1029/2001GC000252](https://doi.org/10.1029/2001GC000252).
- Boatwright, J. (1980). A spectral theory for circular seismic sources; simple estimates of source dimension, dynamic stress drop, and radiated seismic energy, *Bull. Seismol. Soc. Am.* **70**, no. 1, 1–27.
- Bouchon, M. (1981). A simple method to calculate Green's functions for elastic layered media, *Bull. Seismol. Soc. Am.* **71**, no. 4, 959–971, doi: [10.1785/BSSA0710040959](https://doi.org/10.1785/BSSA0710040959).
- Brune, J. N. (1970). Tectonic stress and the spectra of seismic shear waves from earthquakes, *J. Geophys. Res.* **75**, no. 26, 4997–5009, doi: [10.1029/JB075i026p04997](https://doi.org/10.1029/JB075i026p04997).
- Brune, J. N. (1971). Correction to tectonic stress and the spectra of seismic shear waves from earthquakes, *J. Geophys. Res.* **76**, no. 20, 5002, doi: [10.1029/JB076i020p05002](https://doi.org/10.1029/JB076i020p05002).
- Chai, G., S.-H. Yoo, J. Rhie, and T.-S. Kang (2020). Stress-drop scaling of the 2016 Gyeongju and 2017 Pohang earthquake sequences using coda-based methods, *Bull. Seismol. Soc. Am.* **110**, no. 5, 2047–2057, doi: [10.1785/0120200132](https://doi.org/10.1785/0120200132).
- Cluzel, D., L. Jolivet, and J.-P. Cadet (1991). Early middle Paleozoic intraplate orogeny in the Okcheon belt (South Korea): A new insight on the Paleozoic buildup of East Asia, *Tectonics* **10**, no. 6, 1130–1151, doi: [10.1029/91TC00866](https://doi.org/10.1029/91TC00866).
- Daniels, C., Z. Peng, Q. Wu, S. Ni, X. Meng, D. Yao, L. S. Wagner, and M. Fischer (2019). The 15 February 2014 Mw 4.1 South Carolina earthquake sequence: Aftershock productivity, hypocentral depths, and stress drops, *Seismol. Res. Lett.* **91**, no. 1, 452–464, doi: [10.1785/0220190034](https://doi.org/10.1785/0220190034).
- Eshelby, J. D. (1957). The determination of the elastic field of an ellipsoidal inclusion, and related problems, *Proc. Math. Phys. Sci.* **241**, no. 1226, 376–396, doi: [10.1098/rspa.1957.0133](https://doi.org/10.1098/rspa.1957.0133).
- Fan, W., and P. M. Shearer (2016). Local near instantaneously dynamically triggered after-shocks of large earthquakes, *Science* **353**, no. 6304, 1133–1136, doi: [10.1126/science.aag0013](https://doi.org/10.1126/science.aag0013).
- Gephart, J. W. (1990). FMSI: A FORTRAN program for inverting fault/slakenside and earthquake focal mechanism data to obtain the regional stress tensor, *Comput. Geosci.* **16**, 953–989, doi: [10.1016/0098-3004\(90\)90105-3](https://doi.org/10.1016/0098-3004(90)90105-3).
- Helmstetter, A., Y. Y. Kagan, and D. D. Jackson (2005). Importance of small earthquakes for stress transfers and earthquake triggering, *J. Geophys. Res.* **110**, no. B5, doi: [10.1029/2004JB003286](https://doi.org/10.1029/2004JB003286).
- Im, K., D. Elsworth, C. Marone, and J. Leeman (2017). The impact of frictional healing on stick-slip recurrence interval and stress drop: Implications for earthquake scaling, *J. Geophys. Res.* **122**, no. 12, 10,102–10,117, doi: [10.1002/2017JB014476](https://doi.org/10.1002/2017JB014476).
- International Seismological Centre (ISC) (2023). International Seismological Centre, online bulletin, doi: [10.31905/D808B830](https://doi.org/10.31905/D808B830).
- Korea Institute of Geoscience and Mineral Resources (KIGAM) (2019). Geologic map, Andong sheet 1:250000, Korea Institute of Geoscience and Mineral Resources, doi: [10.22747/data.20230712.5013](https://doi.org/10.22747/data.20230712.5013).
- Kim, K. H., J.-H. Ree, Y. Kim, S. Kim, S. Kang, and W. Seo (2018). Assessing whether the 2017 Mw 5.4 Pohang earthquake in South Korea was an induced event, *Science* **360**, no. 6392, 1007–1009, doi: [10.1126/science.2023.104369](https://doi.org/10.1126/science.2023.104369).
- Kim, K. H., and R. Van der Voo (1990). Jurassic and Triassic paleomagnetism of South Korea, *Tectonics* **9**, no. 4, 699–717, doi: [10.1029/TC009i004p00699](https://doi.org/10.1029/TC009i004p00699).
- Kim, S. J., and S. G. Kim (1983). A study on the crustal structure of South Korea by using seismic waves, *J. Korean Inst. Mining Geol.* **16**, no. 1, 51–61.
- Kim, W.-Y., H. Choi, and M. Noh (2010). The 20 January 2007 Odaesan, Korea, earthquake sequence; reactivation of a buried strike-slip fault? *Bull. Seismol. Soc. Am.* **100**, no. 3, 1120–1137, doi: [10.1785/0120090069](https://doi.org/10.1785/0120090069).
- King, G., R. S. Stein, and J. Lin (1994). Static stress changes and the triggering of earthquakes, *Bull. Seismol. Soc. Am.* **84**, no. 3, 935–953.
- Klein, F. W. (1978). Hypocenter location program HYPOINVERSE: Part I. Users guide to versions 1, 2, 3, and 4. Part II. Source listings and notes, *U.S. Geol. Surv. Open-File Rept.* **78-694**, doi: [10.3133/ofr78694](https://doi.org/10.3133/ofr78694).
- Korea Meteorological Administration (KMA) (2012). Historical earthquake records in Korea (2~1904), Korea Meteorological Administration, available at http://www.nims.go.kr/?sub_num=747&state=view&idx=440 (last accessed February 2022).
- Lee, K. (2010). Comments on seismicity and crustal structure of the Korean Peninsula, *Geophys. Geophys. Explor.* **13**, 256–267.
- Lim, H., K. Deng, Y. H. Kim, J.-H. Ree, T.-R. A. Song, and K.-H. Kim (2020). The 2017 Mw 5.5 Pohang earthquake, South Korea, and poroelastic stress changes associated with fluid injection, *J. Geophys. Res.* **125**, no. 6, e2019JB019134, doi: [10.1029/2019JB019134](https://doi.org/10.1029/2019JB019134).
- Madariaga, R. (1976). Dynamics of an expanding circular fault, *Bull. Seismol. Soc. Am.* **66**, no. 3, 639–666, doi: [10.1785/BSSA0660030639](https://doi.org/10.1785/BSSA0660030639).
- McLaskey, G. C., A. M. Thomas, S. D. Glaser, and R. M. Nadeau (2012). Fault healing promotes high-frequency earthquakes in laboratory experiments and on natural faults, *Nature* **491**, no. 7422, 101–104, doi: [10.1038/nature11512](https://doi.org/10.1038/nature11512).
- Michael, A. J. (1984). Determination of stress from slip data: faults and folds, *J. Geophys. Res.* **89**, no. B13, 11,517–11,526, doi: [10.1029/JB089iB13p11517](https://doi.org/10.1029/JB089iB13p11517).
- Onwuemeke, J., Y. Liu, and R. M. Harrington (2018). Earthquake stress drop in the Charlevoix seismic zone, Eastern Canada, *Geophys. Res. Lett.* **45**, no. 22, 12,226–12,235, doi: [10.1029/2018GL079382](https://doi.org/10.1029/2018GL079382).
- Park, S.-I. (2005). Stratigraphy and Geological Structure of the Ongcheon Supergroup in the Jogok area, Goesan, Korea, *M.S. Thesis*, Seoul National University, Seoul, Korea.
- Pennington, C. N., X. Chen, R. E. Abercrombie, and Q. Wu (2021). Cross validation of stress drop estimates and interpretations for the 2011 Prague, OK, earthquake sequence using multiple methods, *J. Geophys. Res.* **126**, e2020JB020888, doi: [10.1029/2020JB020888](https://doi.org/10.1029/2020JB020888).
- Prieto, G. A. (2022). Multitaper: A multitaper spectrum analysis package in Python, *Seismol. Res. Lett.* **93**, no. 3, 1922–1929, doi: [10.1785/0220210332](https://doi.org/10.1785/0220210332).
- Rhee, H. M., and D. H. Sheen (2016). Lateral variation in the source parameters of earthquakes in the Korean Peninsula, *Bull. Seismol. Soc. Am.* **106**, no. 5, 2266–2274, doi: [10.1785/0120160085](https://doi.org/10.1785/0120160085).

- Ross, Z. E., H. Kanamori, and E. Hauksson (2017). Anomalously large complete stress drop during the 2016 Mw 5.2 Borrego Springs earthquake inferred by waveform modeling and near-source aftershock deficit, *Geophys. Res. Lett.* **44**, 5994–6001, doi: [10.1002/2017GL073338](https://doi.org/10.1002/2017GL073338).
- Saikia, C. K. (1994). Modified frequency-wavenumber algorithm for regional seismograms using Filon's quadrature: Modelling of Lg waves in eastern North America, *Geophys. J. Int.* **118**, 142–158, doi: [10.1111/j.1365-246X.1994.tb04680.x](https://doi.org/10.1111/j.1365-246X.1994.tb04680.x).
- Schaff, D. P., G. H. Bokelmann, W. L. Ellsworth, E. E. Zanzerkia, F. Waldhauser, and G. C. Beroza (2004). Optimizing correlation techniques for improved earthquake location, *Bull. Seismol. Soc. Am.* **94**, no. 2, 705–721, doi: [10.1785/0120020238](https://doi.org/10.1785/0120020238).
- Sheen, D.-H., K. J. Seo, S. Kim, B. Kim, Y. Hong, and A.-H. Byun (2023). A rapid and automatic procedure for seismic analysis based on deep learning and template matching: a case study on the M 4.1 Goesan earthquake on October 29, 2022, *J. Geol. Soc. Korea* **59**, no. 2, doi: [10.14770/jgsk.2023.010](https://doi.org/10.14770/jgsk.2023.010).
- Shi, J., W.-Y. Kim, and P. G. Richards (1998). The corner frequencies and stress drops of intraplate earthquakes in the northeastern United States, *Bull. Seismol. Soc. Am.* **88**, no. 2, 531–542, doi: [10.1785/BSSA0880020531](https://doi.org/10.1785/BSSA0880020531).
- Soh, I., C. Chang, J. Lee, T.-K. Hong, and E.-S. Park (2018). Tectonic stress orientations and magnitudes, and friction of faults, deduced from earthquake focal mechanism inversions over the Korean Peninsula, *Geophys. J. Int.* **213**, no. 2, 1360–1373, doi: [10.1093/gji/ggy061](https://doi.org/10.1093/gji/ggy061).
- Song, S.-G., C.-S. Cho, I.-S. Lim, H. Lim, M. Son, H.-S. Kim, Y.-W. Yun, T.-S. Oh, J.-H. Choi, Y. Cheon, et al. (2022). 2022 Goesan earthquake report, Korea Institute of Geosciences and Mineral Resources, 25 pp, available at https://www.kigam.re.kr/gallery.es?mid=a4040300000&bid=0041&list_no=3289&act=view (last accessed August 2023) (in Korean).
- Toda, S., R. S. Stein, and J. Lin (2011). Widespread seismicity excitation throughout central Japan following the 2011 M = 9.0 Tohoku earthquake and its interpretation by Coulomb stress transfer, *Geophys. Res. Lett.* **38**, no. 7, L00G03, doi: [10.1029/2011GL047834](https://doi.org/10.1029/2011GL047834).
- Viegas, G., R. E. Abercrombie, and W.-Y. Kim (2010). The 2002 M5 Au Sable Forks, NY, earthquake sequence: Source scaling relationships and energy budget, *J. Geophys. Res.* **115**, no. B7, doi: [10.1029/2009JB006799](https://doi.org/10.1029/2009JB006799).
- Waldhauser, F. (2001). hypoDD—A program to compute double-difference hypocenter locations, *U.S. Geol. Surv. Open-File Rept. 2001-113*, doi: [10.7916/D8SN072H](https://doi.org/10.7916/D8SN072H).
- Waldhauser, F., and W. L. Ellsworth (2000). A double-difference earthquake location algorithm: Method and application to the northern Hayward fault, California, *Bull. Seismol. Soc. Am.* **90**, 1353–1368, doi: [10.1785/0120000006](https://doi.org/10.1785/0120000006).
- Wu, Q., and M. Chapman (2017). Stress-drop estimates and source scaling of the 2011 mineral, Virginia, mainshock and aftershocks, *Bull. Seismol. Soc. Am.* **107**, no. 6, 2703–2720, doi: [10.1785/0120170098](https://doi.org/10.1785/0120170098).
- Wu, Q., M. Chapman, and X. Chen (2018). Stress-drop variations of induced earthquakes in Oklahoma, *Bull. Seismol. Soc. Am.* **108**, 1107–1123, doi: [10.1785/0120170335](https://doi.org/10.1785/0120170335).
- Zoback, M. L., and M. Magee (1991). Stress magnitudes in the crust: Constraints from stress orientation and relative magnitude data, *Phil. Trans. Roy. Soc. Lond. A* **337**, no. 1645, 181–194, doi: [10.1098/rsta.1991.0115](https://doi.org/10.1098/rsta.1991.0115).

Manuscript received 19 April 2023

Published online 30 August 2023